Scalewise invariant analysis of the anisotropic Reynolds stress tensor for atmospheric surface layer and canopy sublayer turbulent flows

Peter Brugger,[1,*] Gabriel G. Katul,[2,3,1] Frederik De Roo,[1] Konstantin Kröniger,[1] Eyal Rotenberg,[4] Shani Rohatyn,[4] and Matthias Mauder[1]

[1]*Karlsruhe Institute of Technology (KIT), Institute of Meteorology and Climate Research - Atmospheric Environmental Research (IMK-IFU), Kreuzeckbahnstraße 19, 82467 Garmisch-Partenkirchen, Germany*

[2]*Nicholas School of the Environment, Box 80328, Duke University, Durham, North Carolina 27708, USA*

[3]*Department of Civil and Environmental Engineering, Duke University, Durham, North Carolina 27708, USA*

[4]*Weizmann Institute of Science (WIS), Faculty of Chemistry, Department of Earth and Planetary Sciences, 234 Herzl Street, Rehovot 7610001, Israel*

(Received 21 December 2017; published 24 May 2018)

Anisotropy in the turbulent stress tensor, which forms the basis of invariant analysis, is conducted using velocity time series measurements collected in the canopy sublayer (CSL) and the atmospheric surface layer (ASL). The goal is to assess how thermal stratification and surface roughness conditions simultaneously distort the scalewise relaxation towards isotropic state from large to small scales when referenced to homogeneous turbulence. To achieve this goal, conventional invariant analysis is extended to allow scalewise information about relaxation to isotropy in physical (instead of Fourier) space to be incorporated. The proposed analysis shows that the CSL is more isotropic than its ASL counterpart at large, intermediate, and small (or inertial) scales irrespective of the thermal stratification. Moreover, the small (or inertial) scale anisotropy is more prevalent in the ASL when compared to the CSL, a finding that cannot be fully explained by the intensity of the mean velocity gradient acting on all scales. Implications to the validity of scalewise Rotta and Lumley models for return to isotropy as well as advantages to using barycentric instead of anisotropy invariant maps for such scalewise analysis are discussed.

DOI: 10.1103/PhysRevFluids.3.054608

I. INTRODUCTION

The classical treatment of turbulence in the atmospheric surface layer (ASL) and the roughness sublayer (CSL) above canopies has primarily focused on distortions to the mean velocity profile caused by the presence of roughness elements and thermal stratification [1–9]. Surface roughness effects and thermal stratification modify the components of the Reynolds stress tensor, as evidenced by a large number of experiments and simulations [5,10–19]. These modifications are expected to lead to differences in kinetic energy distribution among velocity components comprising the stress tensor. Such differences in energy anisotropy has been previously used to explore the sensitivity of turbulent structures to surface boundary conditions such as roughness changes [20–25] or thermal stratification [26]. However, the route of how the anisotropy at large scales relaxes to quasi-isotropic state at small scales remains a subject of research [27–31]. The juxtaposition of these questions and studies to ASL and CSL turbulence using field measurements is the main motivation for the work here.

Exchanges of turbulent kinetic energy among the three spatial components occur through interactions between fluctuating velocities and pressure. Starting from an anisotropic stress tensor

*peter.brugger@kit.edu

$\overline{u_i u_j}$, these exchanges have been labeled as return to isotropy; when mean flow gradients are removed or suppressed, they describe the expected state that turbulence relaxes to. Here, u_i are the turbulent or fluctuating velocity components along x_i, where x_1 (or x), x_2 (or y), and x_3 (or z) represent the longitudinal, lateral, and vertical directions, respectively, the overbar denotes time averaging, and $\overline{u_i} = 0$. Much progress has been made by exploring connections between $\overline{u_i u_j}$ and the so-called invariant analysis [22,30,32–36]. Such connections resulted in nonlinear models for the slow part of the pressure-strain correlation and highlighted distinct routes along which turbulence relaxes to isotropic conditions [27,33,34]. These routes have been succinctly summarized in what are labeled as anisotropy invariant maps (AIM), proposed by Lumley [33,34]. Invariant analysis is based on the anisotropic second-order normalized stress tensor related to $\overline{u_i u_j}$ by

$$a_{ij} = \frac{\overline{u_i u_j}}{2k} - \frac{1}{3}\delta_{ij}, \quad k = \frac{\overline{u_m u_m}}{2}, \tag{1}$$

where k is the mean turbulent kinetic energy and δ_{ij} is the Kronecker delta. This tensor has three invariants: $I_1 = a_{ii} = 0$, here and $I_2 = a_{ij}a_{ji}$ and $I_3 = a_{ij}a_{jn}a_{ni}$, which are independent of the coordinate rotation of the reference system and can be linked to the eigenvalues of a_{ij}. Invariant maps feature I_3 (abscissa) versus $-I_2$ (ordinate) along with bounds imposed by realizability constraints on $\overline{u_i u_j}$ (e.g., $\det[a_{ij}] \geqslant 0$, where $\det[\cdot]$ is the determinant). The I_2 represents the degree of anisotropy whereas I_3 represents the nature (or topology) of the anisotropy. The AIM approach suggests that anisotropy in $\overline{u_i u_j}$ may be 1-component (rodlike energy distribution), 2-component (disklike energy distribution), or 3-component, of which the isotropic state (spherical energy distribution) is a limiting case. Depending on the sign of I_3, progression from 1-component or 2-component to 3-component follows an axisymmetric expansion or contraction on the AIM when the source of inhomogeneity (e.g., mean flow gradients) is removed until isotropy is achieved [34]. As noted earlier, the AIM domain bounds all realizable Reynolds stress invariants [22,34,37,38], thereby making AIM an effective visual tool to track anisotropy at different heights in boundary layer turbulence. In fact, the AIM proved to be effective at demonstrating that rough-wall turbulence appears more isotropic than its smooth-wall counterpart for the same Reynolds numbers [21]. Experiments and simulations [25] also reported that the AIM signature for smooth wall turbulence appears well defined and robust to variations in Reynolds number. The same experiments further showed that turbulent flows over three-dimensional (3D) k-type roughness appear more isotropic than flows over their 2D k-type roughness counterparts throughout the boundary layer [25].

An alternative to the AIM representation is the barycentric map (BAM), which offers a number of advantages over AIM, such as nondistored visualization of anisotropy and weighting of the limiting states, as discussed elsewhere [32]. However, AIM and BAM representations are connected by transformations derived from the three eigenvalues of a_{ij}. Invariant analysis in a_{ij} assumes that anisotropy is inherently a large-scale feature, and finer scales become isotropic and decoupled from their anisotropic large scales counterpart. How anisotropy in a_{ij} is destroyed as eddy sizes or scales become smaller remains a subject of inquiry, especially in vertically inhomogeneous flows characterizing the ASL and CSL of the atmosphere. The ASL and CSL experience mechanical production of k through interactions between the turbulent shear stress and the mean velocity profile. However, additional sources (or sinks) of k occur through surface heating (or cooling) and their associated thermal stratification. Above and beyond these two processes, canopy roughness effects introduce additional length scales (e.g., adjustment length and shear length scales) when describing flow statistics in the CSL [5,39].

Two early pioneering attempts to extend invariant analysis across scales were conducted in the Fourier domain. One utilized numerical simulations of isotropic turbulence [28]. The other considered 3-component velocity time series collected in a pipe at multiple distances from the pipe wall and at two bulk Reynolds numbers [23]. The simulation study showed that small-scale anisotropy in Reynolds stresses persisted and was traced back to nonlocal triad interactions that appear not efficient at destroying an initial spanwise energy injection. The pipe flow experiments showed that, at large scales, near-wall structures exhibit "rod-like" (or prolate) energy distribution whereas "disk-like"

(or oblate) energy distribution characteristics were reported as the buffer region is approached. Approximate isotropic states were reported as the pipe center is approached, where the mean velocity gradients approach zero (by virtue of symmetry). Another recent study [26] also extended aspects of invariant analysis across scales in the Fourier domain to explore how thermal stratification modifies isotropic and anisotropic states above an urban canopy. This work showed that the relaxation rate towards local isotropy varies with thermal stratification. Specifically, unstable atmospheric stability appears to be closer to the isotropic state than its near-neutral or stable counterpart at a given scale or wave number. A relation was suggested between the scale over which maximum isotropy is attained and an outer length scale derived from temperature statistics [26].

The work here uses invariant analysis across scales in the ASL and CSL to explore the simultaneous role of roughness contrast and thermal stratification on anisotropy relaxation towards quasi-isotropic conditions. How anisotropy in a_{ij} produced at large scales varies with thermal stratification in the ASL and CSL and how such a large-scale anisotropic state relaxes to quasi-isotropic conditions at progressively smaller scales frame the scope of the work. The novelties of the analysis proposed here over prior work [23,26] are that (1) velocity differences in physical space are used instead of spectral and cospectral analysis, and (2) both AIM and BAM measures of anisotropy are employed and their outcome compared to conventional local isotropy analysis. Advantages to conducting the analysis in physical space instead of spectral space are discussed.

With regards to the experimental design, the 3-component velocity time series were simultaneously collected in the CSL above a tall forest and in the ASL above an adjacent desert-like shrubland. The runs spanned a wide range of atmospheric stability conditions as characterized by the atmospheric stability parameter. Distances to the surface or zero-plane displacement (in the case of the forest) were similar for both setups and were chosen to be commensurate with the aforementioned experiment on the urban surface layer [26]. It is envisaged that the analysis reported here offers a new perspective on the relative sensitivity of turbulent structures to roughness modifications and thermal stratification, especially at the crossover from large (or integral) scales to inertial scales.

II. METHOD OF ANALYSIS

A. Definitions and nomenclature

Any three-dimensional second-rank tensor σ_{ij} has three independent invariant quantities associated with it, which can be determined from the eigenvalues of σ_{ij}. The eigenvalues (λ) are computed from the determinant $\det[\sigma_{ij} - \lambda\delta_{ij}] = 0$. Expanding the determinant of the matrix

$$\begin{bmatrix} \sigma_{11} - \lambda & \sigma_{12} & \sigma_{13} \\ \sigma_{21} & \sigma_{22} - \lambda & \sigma_{23} \\ \sigma_{31} & \sigma_{32} & \sigma_{33} - \lambda \end{bmatrix}$$

and setting it to zero yields the characteristic equation that defines the invariants and is given by [40]

$$\det[\sigma_{ij} - \lambda\delta_{ij}] = -\lambda^3 + I_1\lambda^2 - I_2\lambda + I_3 = 0, \tag{2}$$

where

$$I_1 = \sigma_{kk} = \mathrm{tr}[\sigma], \tag{3}$$

$$I_2 = \tfrac{1}{2}(\sigma_{ii}\sigma_{jj} - \sigma_{ij}\sigma_{ji}), \tag{4}$$

$$I_3 = \det[\sigma_{ij}], \tag{5}$$

with tr[·] being the trace of σ_{ij}. When $\sigma_{ij} = a_{ij}$, symmetry insures that Eq. (2) has three real roots (the eigenvalues) labeled as λ_1, λ_2, and λ_3. The principal stresses are defined as components of σ_{ij} when the basis is changed so that the shear stress components become zero and σ_{ij} becomes a 3×3 diagonal matrix whose elements are σ_1, σ_2, and σ_3. These principal stresses are the three eigenvalues

ordered by magnitude using $\sigma_1 = \max(\lambda_1,\lambda_2,\lambda_3)$, $\sigma_3 = \min(\lambda_1,\lambda_2,\lambda_3)$, and $\sigma_2 = I_1 - \sigma_1 - \sigma_3$. The σ_1, σ_2, and σ_3 are independent of the coordinate basis in which the components of σ_{ij} are originally derived, which is advantageous in ASL and CSL field studies where large variations in wind directions are unavoidable. Applying the diagonal form of σ_{ij} to the definitions of the three invariants given by Eq. (2) yields the following simplified expressions:

$$I_1 = \sigma_1 + \sigma_2 + \sigma_3, \tag{6}$$

$$I_2 = \sigma_1\sigma_2 + \sigma_2\sigma_3 + \sigma_3\sigma_1, \tag{7}$$

$$I_3 = \sigma_1\sigma_2\sigma_3. \tag{8}$$

These definitions directly apply to a_{ij} or any other second-rank tensor such as the strain rate [40,41] and others relevant to vorticity and dissipation [20]. One advantage to using a_{ij} here instead of $\overline{u_i u_j}$ for invariant analysis is that $I_1 = \mathrm{tr}[\mathrm{a_{ij}}] = \mathrm{a_{11}} + \mathrm{a_{22}} + \mathrm{a_{33}} = 0$ and only the second and third invariants are required.

The BAM framework makes use of the fact that a_{ij} can be expressed as a linear combination of three limiting states (1-component, 2-component, or 3-component). That is, a_{ij} can be decomposed into $C_{1c}a_{1c} + C_{2c}a_{2c} + C_{3c}a_{3c}$, where C_{1c}, C_{2c}, and C_{3c} are determined from the eigenvalues using [32]

$$C_{1c} = \lambda_1 - \lambda_2, \tag{9}$$

$$C_{2c} = 2(\lambda_2 - \lambda_3), \tag{10}$$

$$C_{3c} = 3\lambda_3 + 1, \tag{11}$$

and a_{1c}, a_{2c}, and a_{3c} are 3×3 diagonal matrices with diagonal elements $[2/3,-1/3,-1/3]$ (1-component limiting state), $[1/6,1/6,-1/3]$ (2-component limiting state), and $[0,0,0]$ (3-component limiting state). In the BAM representation, C_{1c}, C_{2c}, and C_{3c} determined from λ_1, λ_2, and λ_3 indicate how much each turbulent state is contributing to a point situated in the map. The map itself can be constructed within an equilateral triangle with vertices being the three limiting states defined by coordinates $(x_{1c},y_{1c}) = (1,0)$, $(x_{2c},y_{2c}) = (-1,0)$, and $(x_{3c},y_{3c}) = (0,\sqrt{3})$. Once these limiting states are set, a normalization is applied so that $C_{1c} + C_{2c} + C_{3c} = 1$ and the coordinates of any point on the map $(x_{\mathrm{BAM}}, y_{\mathrm{BAM}})$ can be determined from

$$x_{\mathrm{BAM}} = C_{1c}x_{1c} + C_{2c}x_{2c} + C_{3c}x_{3c}, \tag{12}$$

$$y_{\mathrm{BAM}} = C_{1c}y_{1c} + C_{2c}y_{2c} + C_{3c}y_{3c}. \tag{13}$$

As discussed elsewhere [32], an equilateral triangle shaped BAM does not introduce any visual bias of the limiting states as is the case for the AIM. Randomly distributed points within BAM, when converted to AIM, result in visual clustering near the isotropic or 3-component state primarily because of the nonlinearity in the transformation from BAM to AIM.

B. Measures of anisotropy

A scalar measure of anisotropy in the AIM is the shortest or linear distance to the isotropic state. This distance was determined from I_2 and I_3 via [22,33]

$$F = 1 + 27I_3 + 9I_2. \tag{14}$$

Isotropic turbulence is strictly attained when both $I_2 = I_3 = 0$ and $F = 1$, whereas $F = 0$ occurs along the linear boundary describing the 2-component state. The distance F was reported to be a function of distance from a solid boundary for various turbulent boundary layer flows [22–25]. At all

distances from the boundary, F was smaller for turbulent flows over smooth walls when compared to all types of rough-wall cases [24,25].

In the BAM, the distance to the isotropic state is [32]

$$C_{\text{ani}} = -3\lambda_3. \tag{15}$$

This measure has not been extensively used before, and is employed along with F for the data collected in the ASL and CSL.

C. Scalewise analysis

The scalewise analysis of AIM and BAM uses the structure function approach (in physical or r space) instead of Fourier space. The overall premise is similar to what was proposed earlier [28] except that structure functions ensure integrability and minimize other limitations discussed elsewhere for spectral and co-spectral versions [23]. The premise of the scalewise AIM or BAM analysis is to replace $\overline{u_i u_j}$ by

$$D_{ij}(r) = \tfrac{1}{2}\overline{\Delta u_i(r)\Delta u_j(r)}, \tag{16}$$

where $\Delta u_k(r) = u_k(x+r) - u_k(x)$, and r is the separation distance along the longitudinal (or x_1) direction determined from time increments and Taylor's frozen turbulence hypothesis [42,43], which is conventional when interpreting time series in field experiments. Equation (16) has a number of desirable limits. To illustrate, consider its expansion given as

$$D_{ij}(r) = \tfrac{1}{2}(\overline{u_i(x+r)u_j(x+r)} + \overline{u_i(x)u_j(x)}) - \tfrac{1}{2}(\overline{u_i(x+r)u_j(x)} + \overline{u_i(x)u_j(x+r)}). \tag{17}$$

For planar homogeneous flows and at $r/L_I \gg 1$, $D_{ij}(r) \approx \overline{u_i(x)u_j(x)}$ [or $D_{ij}(r) \approx \overline{u_i(x+r)u_j(x+r)}$], where L_I is the integral length scale of the flow (to be defined later). Hence, $D_{ij}(r)$ recovers all the properties of the stress tensor at large scales. For $r \to 0$, $D_{ij}(r) \to 0$ and ensures no energy and stress contributions at very small scales. The use of $D_{ij}(r)$ is rather convenient because expected scaling laws for inertial subrange eddies are known. For example, when $i = 1$ and $j = 1$, $D_{11}(r)$ becomes the longitudinal velocity structure function, which measures the integrated energy content at scale r. It is noted here that $rdD_{11}(r)/dr \propto k_1 E_{11}(k_1)$, where k_1 is the one-dimensional wave number along direction x_1 and $E_{11}(k_1)$ is the longitudinal velocity energy spectrum. Likewise, for $r/L_I \gg 1$, $D_{11}(r) \to \overline{u_1 u_1}$. Because structure functions measure integrated energy content at a given scale r, the singularity issues in Fourier domain noted elsewhere [23] are bypassed. For locally isotropic turbulence and for $\eta/L_I \ll r/L_I \ll 1$, Kolmogorov (or K41) scaling is expected to hold in the ASL and yields the following for the componentwise structure functions:

$$D_{11}(r) = C_{o,1}\overline{\epsilon}^{2/3} r^{2/3}, \tag{18}$$

$$D_{22}(r) = C_{o,2}\overline{\epsilon}^{2/3} r^{2/3}, \tag{19}$$

$$D_{33}(r) = C_{o,3}\overline{\epsilon}^{2/3} r^{2/3}, \tag{20}$$

where $\eta = (\nu^3/\overline{\epsilon})^{1/4}$ is the Kolmogorov microscale, ν is the fluid kinematic viscosity, $C_{o,2} = C_{o,3} = (4/3)C_{o,1}$, $C_{o,1} = 2$, and $\overline{\epsilon}$ is the mean dissipation rate of k. One undesirable outcome to using $D_{ij}(r)$ is its nonzero trace at any r. As was the case with a_{ij} and $\overline{u_i(x)u_j(x)}$, this outcome may be circumvented by evaluating

$$A_{ij}(r) = \frac{D_{ij}(r)}{D_{kk}(r)} - \frac{1}{3}\delta_{ij}. \tag{21}$$

The AIM and BAM as well as $F(r)$ and $C_{\text{ani}}(r)$ can now be computed for the ASL and CSL velocity time series once the eigenvalues of $D_{ij}(r)$ or $A_{ij}(r)$ are determined for each $r > 0$.

D. Comparison with a reference model

To compare the computed scalewise variations of I_2 and I_3 in the CSL and ASL with a well-studied turbulent state, homogeneous turbulence (i.e., lacking any mean flow gradients) is selected as a reference. Once the mean flow gradients are removed for this reference state, the decay rates of I_2 and I_3 are shown to reasonably follow a quadratic model given by [27]

$$\frac{dI_2}{d\tau} = -2(B_1 - 2)I_2 + 2B_2 I_3, \tag{22}$$

$$\frac{dI_3}{d\tau} = -3(B_1 - 2)I_3 + \frac{1}{2}B_2 I_2^2, \tag{23}$$

where τ is a relaxation time scale, and $B_1 = 3.4$ and $B_2 = 3(B_1 - 2)$ are constants determined by fitting this model to a wide range of experiments. For $B_2 = 0$, this system recovers the Lumley model [33] (i.e., uncoupled equations), and for $B_2 = 0$ and $I_3 = 0$, the classical Rotta model is recovered. Hence, finite B_2 and I_3 offer a clear indication that the linear Rotta model may not be adequate to describe the trajectory towards isotropy. The two ordinary differential equations can now be combined to yield

$$\frac{dI_2}{dI_3} = \frac{-2(B_1 - 2)I_2 + 2B_2 I_3}{-3(B_1 - 2)I_3 + \frac{1}{2}B_2 I_2^2}, \tag{24}$$

which can be solved to yield $-I_2$ as a function of I_3 (i.e., the trajectory on the AIM) without requiring the determination of time τ provided τ is sufficiently large to attain the isotropic state. The trajectories of this model (in AIM or BAM) are simply computed here to illustrate how homogeneous turbulence relaxes to the isotropic state once the mean flow gradients (that are prevalent in ASL and CSL) are suppressed. The initial conditions to equation (24) are the measured I_2 and I_3 in the CSL or ASL as determined for $r/L_I \gg 1$.

III. EXPERIMENTS

A. Research site

The experiments were conducted at the Yatir Forest in southern Israel, which is a planted evergreen pine forest surrounded by a sparse desert-like shrubland [44]. The trees were planted in the late 1960s and now cover an approximate area of 28 km^2 [44]. The primary tree species of the forest is *Pinus halepensis* and the shrubland has scattered herbaceous annuals and perennials (mainly *Sarcopoterium spinosum*). The albedo of the forest is low (=12.5%) when compared to the shrubland (=33.7%). In the absence of latent heat fluxes (as is the case in the extensive dry season), this albedo contrast leads to sensible heat fluxes up to 800 W m^{-2} during the day over the forest, which can be twice as high as those of the surrounding shrubland [45]. The higher roughness length of the forest also creates friction velocities (u_*) of up to 0.8 m s^{-1}, which are twice as high as those above the shrubland [45]. These sensible heat flux and friction velocity differences between the forest and shrubland do impact the generation of k. To illustrate, a stationary and planar-homogeneous flow at high Reynolds number in the absence of subsidence is considered. The k budget for such an idealized flow is

$$\frac{\partial k}{\partial t} = 0 = -\overline{u_1 u_3}\frac{dU}{dz} + \beta_o g\overline{u_3 T'} + P_D + T_T - \bar{\epsilon}, \tag{25}$$

where t is time, and the five terms on the right-hand side of Eq. (25) are mechanical production, buoyant production (or destruction), pressure transport, turbulent transport of k, and viscous dissipation of k, respectively; β_o is the thermal expansion coefficient for air ($\beta_o = 1/T$, T is mean air temperature and T' is temperature fluctuation), g is the gravitational acceleration, $-\overline{u_1 u_3} = u_*^2$ is the turbulent kinematic shear stress near the surface, $\overline{u_3 T'}$ is the kinematic sensible heat flux from (or to) the surface, and U is the mean longitudinal velocity. The $\rho_a C_p \overline{u_3 T'}$ defines the sensible heat flux in energy units (W m^{-2}), with ρ_a and C_p being the mean air density and the specific heat

capacity of dry air at constant pressure, respectively. When $\overline{u_3T'} > 0$, buoyancy is responsible for the generation of k and the flow is classified as unstable. When $\overline{u_3T'} < 0$, the flow is classified as stable and buoyancy acts to diminish the mechanical production of k. The relative significance of the mechanical production to the buoyancy generation (or destruction) in the TKE budget may be expressed as [10,13,14]

$$-\overline{u_1u_3}\frac{dU}{dz} + \beta_o g\overline{u_3T'} = \frac{u_*^3}{\kappa z}\left[\phi_m(\zeta) + \frac{\kappa z\beta_o g\overline{u_3T'}}{u_*^3}\right] = \frac{u_*^3}{\kappa z}[\phi_m(\zeta) - \zeta], \tag{26}$$

where

$$\frac{\kappa z}{u_*}\frac{dU}{dz} = \phi_m(\zeta), \quad \zeta = \frac{z}{L}, \quad L = -\frac{u_*^3}{\kappa g\beta_o\overline{u_3T'}}, \tag{27}$$

and $\phi_m(\zeta)$ is known as a stability correction function reflecting the effects of thermal stratification on the mean velocity gradient [$\phi_m(0) = 1$ recovers the von Karman–Prandtl logarithmic law], $\kappa \approx 0.4$ is the von Karman constant, and L is known as the Obukhov length [46] as described by the Monin and Obukhov similarity theory [1,2,7,9]. The physical interpretation of L is that it is the height at which mechanical production balances the buoyant production or destruction when $\phi_m(\zeta)$ does not deviate appreciably from unity. For a neutrally stratified atmospheric flow, $|L| \to \infty$ and $|\zeta| \to 0$. The sign of L reflects the direction of the heat flux, with negative values of L corresponding to upward heat fluxes (unstable atmospheric conditions) and positive values L corresponding to downward heat flux (stable atmosphere).

B. Instruments and measurements

High-frequency measurements of the turbulent velocity components were conducted concurrently in the CSL over the forest and the ASL of the surrounding shrubland desert ecosystem. The measurements in the ASL were conducted northwest of the forest above the shrubland with a mobile mast positioned at latitude 31.3757°, longitude 35.0242°, and 620 m above sea level. The mast was equipped with a R3-100 ultrasonic anemometer from Gill Instruments Ltd. (Lymington, Hampshire, UK) sampling three orthogonal velocity components with a frequency of 20 Hz. The ultrasonic anemometer was mounted at a height of 9 m above ground surface. The measurements in the CSL were conducted above the forest canopy with a R3-50 ultrasonic anemometer from Gill Instruments with a measurement frequency of 20 Hz (latitude 31.3453°, longitude 35.0522°, 660 m above sea level). The manufacturer states for both ultrasonic anemometers an accuracy <1% for mean wind speeds below 32 m s^{-1}. Wind tunnel and atmospheric comparison to hot-film anemometers showed an accuracy of 2% for the mean wind speed, 9% for variances, and 23% for covariances [47]. The sonic anemometer was mounted 19 m above the ground surface on a meteorological tower. The mean height of the trees around the tower is 10 m, placing the sonic anemometer some 9 m above the canopy top and commensurate to the setup of the urban roughness study previously discussed [26]. The anemometer sonic path length is 0.15 m; hence, separation distances smaller than 0.3 m are not used as they are influenced by instrument averaging. Data from the period 17–23 August 2015 are used here. During this period, the Yatir forest experienced a subtropical ridge, an area of general subsidence in the troposphere connected to the sinking branch of the Hadley cell [48]. The horizontal air pressure gradients were controlled by a heat-induced surface low, the Persian trough, to the east [49]. This led to stationary weather conditions with a main wind direction from the northwest and cloud-free conditions with a radiation driven diurnal cycle of the boundary layer height during the campaign.

C. Post-processing

The measured u_i time series were first separated into nonoverlapping 30-minute runs, and turbulent flow statistics were computed using the 30-minute averaging period per run. Threshold filters of 50 $\mathrm{m\,s^{-1}}$ for the horizontal wind components and 10 $\mathrm{m\,s^{-1}}$ for the vertical component were applied, and spikes were removed by a five-standard-deviation threshold. Then gaps in the time series were linearly interpolated when the total gap length was less than 5% (otherwise the 30-minute run was discarded). The interpolated data set was rotated into the mean wind direction using a standard double rotation ($\overline{u_3} = \overline{u_2} = 0$ and $U \neq 0$) and the mean value was subtracted to obtain turbulent fluctuations. Further quality control was conducted using stationary tests and integral turbulence characteristic tests described elsewhere [50], and only intervals with the best quality metrics were used [51]. For comparison purposes, only intervals where both sites had simultaneous high quality measurements were used. After such post-processing, 65 runs remained for investigating the anisotropy in the ASL and CSL.

IV. RESULTS AND DISCUSSION

To address the study objective, the results are presented as follows: the a_{ij} components computed from Eq. (1) for the ASL and CSL and their dependence on ζ are first presented. Similarities between anisotropy in componentwise turbulent kinetic energy and integral scales along the x_1,x_2,x_3 are also featured. Next, attainment of local isotropy at finer scales is explored by comparing measured $D_{11}(r)$, $D_{22}(r)$, and $D_{33}(r)$ with predictions from K41 scaling and corollary isotropic measures. The scalewise development of the anisotropic stress tensor $[A_{ij}(r)]$ for the ASL and CSL, as determined from Eq. (21), is then discussed using AIM and BAM. Predictions from Eq. (24) are displayed as references to illustrate expected pathways by which $A_{ij}(r)$ approaches its isotropic state with decreasing r for homogeneous turbulence. Finally, the two scalewise measures $F(r)$ and $C_{\mathrm{ani}}(r)$ are presented as a function of r for CSL and ASL flows across a wide range of ζ values. The focus here is on two types of scales: (i) the largest r for which local isotropy is attained, and (ii) the smallest r over which the return to isotropy begins to be efficient. These two scales are then contrasted for ASL and CSL flows and across ζ values, thereby completing the sought objective.

A. Conventional analysis

Unsurprisingly, the computed a_{ij} components exhibit large anisotropy for both ASL and CSL flows. In particular, the streamwise a_{11} and the cross-streamwise a_{22} attain positive values (i.e., more energy than isotropic predictions) as evidenced by Figs. 1(a) and 1(b) and negative values for the vertical a_{33} [Fig. 1(c)] when compared to the expected $Y = 0$ designating the isotropic state. The streamwise and cross-stream components show that the anisotropy for near-neutral conditions in the CSL is between the vertical and streamwise components. The sum of the two horizontal components ($a_{11} + a_{22} = -a_{33}$), which accounts for much of the k, is expected to provide a robust measure of the anisotropy between the horizontal and vertical components. The mean values for a_{33} differ between CSL and ASL at a 95% confidence level, confirming a significantly larger anisotropy in the ASL when compared to its CSL counterpart. The analysis here also shows that a_{33} and a_{23} are not sensitive to variations in ζ for both ASL and CSL flows. The only component of a_{ij} that exhibits variation with ζ is a_{13} in the CSL, which has a slope significantly different from zero at a 95% confidence level. The a_{13} is small in the ASL by comparison to its CSL values. The scatter of most data points in Fig. 1 can be explained by the measurement accuracy, but in the cases of a_{11} and a_{22} the accuracy alone cannot explain the variation and it is likely that nonstationary wind directions affect those components. Direct numerical simulations of homogeneous turbulent shear flows showed more isotropy for weaker shear [52], which agrees with our experiments, where the CSL appears more isotropic and has weaker shear parameter S^* compared to its ASL counterpart for near-neutral conditions. Moreover, the simulation results [52] showed patterns among the components of a_{ij} that are similar to the atmospheric measurements reported in Fig. 1 for a near-neutral ASL. The S^* here varied from 35 to 83 compared to their highest, $S^* = 27$, where $S^* = Sk^2/\epsilon$ with $S = U/(z-d)$.

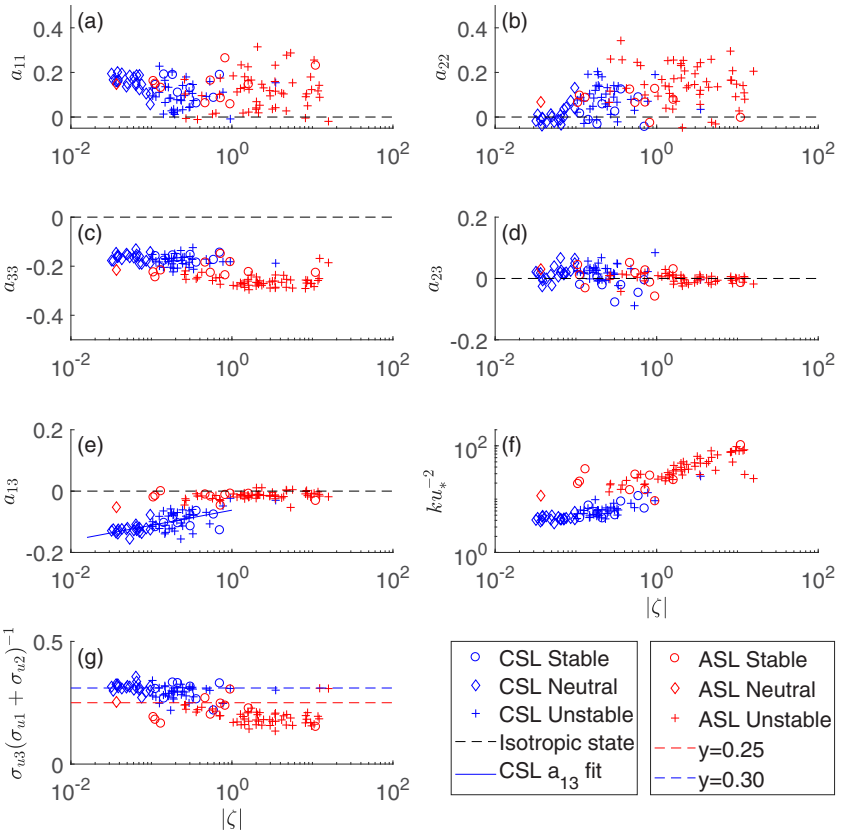

FIG. 1. The measured components of the anisotropy tensor a_{ij} are shown as a function of the absolute value of the stability parameter $|\zeta| = |(z-d)/L|$ [(a), (b), (c), and (e)]. Measurements of the ASL (desert) are red and those of the CSL (forest) are blue. Circles show stable conditions, diamonds are used for near neutral stratification conditions, and crosses denote unstable conditions. The a_{33} shown in panel (c) are significantly larger in the CSL compared to the ASL at a confidence level of 95%. The black dashed line shows the expected value for isotropic turbulence and the solid blue line in panel (e) shows a linear regression of a_{33} for the CSL. The lower right panel (f) shows turbulent kinetic energy k normalized with u_* and the lower left panel (g) shows $\sigma_{u3}(\sigma_{u1}+\sigma_{u2})^{-1}$ together with the expectation for near neutral conditions as dashed lines [5]. Note the larger $\sigma_{u3}(\sigma_{u1}+\sigma_{u2})^{-1}$ for the CSL when compared to the ASL.

Moreover, these simulations do not have a "wall" thereby suppressing any possible wall-blocking likely to be higher in the ASL than the CSL. As earlier noted, the u_*^2 is larger for the CSL when compared to the ASL due to the rougher forest cover. While $\overline{u_3u_3}/u_*^2$ increases with increasing $-\zeta$, $\overline{u_1u_1}/u_*^2$ and $\overline{u_2u_2}/u_*^2$ vary with both $-\zeta$ and $\log_{10}(z/h_{BL})$, where h_{BL} is the boundary layer height as discussed elsewhere [16,17,53–55] with higher values (and fraction of k) in the ASL when compared to the CSL. Separate field experiments suggest that h_{BL} above the forest and the shrubland are comparable [56] (and by design, so are the z values in the CSL and ASL). These findings explain the lower measured k/u_*^2 in the CSL [Fig. 1(f)] when compared to its ASL counterpart given the larger u_* over the forest. While $\overline{u_1u_1}/u_*^2$, $\overline{u_2u_2}/u_*^2$, and $\overline{u_3u_3}/u_*^2$ follow expectations for near-neutral conditions from a mixing layer analogy [5] in the CSL, these flow statistics were higher than expected for the ASL (not shown). A plausible explanation for higher than expected values in the ASL are some topographic variability upwind of the ASL measurement tower. However, the aforementioned topographic variability did not affect the anisotropy appreciably given that canopy sublayer experiments (field and laboratory) collected at $z/h = 1$ yield $\sigma_{u3}(\sigma_{u1}+\sigma_{u2})^{-1} = 0.30$ (with

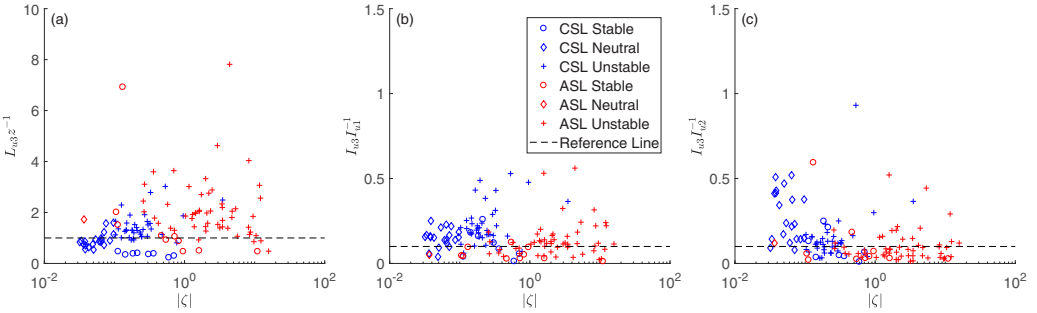

FIG. 2. Normalized length scale $L_{u3}z^{-1}$ (a) and the length scale ratios $L_{u3}L_{u1}^{-1}$ (b) and $L_{u3}L_{u2}^{-1}$ (c) are shown as a function of the absolute value of the stability parameter $|\zeta| = |(z-d)/L|$. Measurements of the ASL (desert) are red and those of the CSL (forest) are blue. Unstable stratification is shown as crosses, near neutral as diamonds, and stable as circles. The dashed line in panels (b) and (c) shows $L_{u3}L_{u1}^{-1} = 0.1$ reported from other experiments [57,58].

$\sigma_{ui} = \sqrt{\overline{u_i u_i}}$) whereas surface layer experiments yield $\sigma_{u3}(\sigma_{u1} + \sigma_{u2})^{-1} = 0.25$, to which ASL and CSL appear to be commensurate for near-neutral conditions [Fig. 1(g)].

To contrast energy anisotropy with eddy size anisotropy along the x_1, x_2, and x_3 directions, the effective eddy sizes for the u_i are determined from the integral time scale I_{ui} and Taylor's frozen turbulence hypothesis [42] using

$$L_{ui} = U I_{ui} = U \int_0^\infty \rho_{ui}(\tau_0) d\tau_0, \tag{28}$$

where $\rho_{ui}(\tau_0)$ is the u_i velocity component autocorrelation function and τ_0 is the time lag. Here, L_{u3} is presumed to be the most restrictive scale given that u_3 is the flow variable most impacted by the presence of a boundary (porous in the CSL and solid in the ASL). The calculations show that L_{u3}/z is on the order of unity for the CSL but higher in the ASL for near-neutral conditions [Fig. 2(a)]. As expected, L_{u3}/L_{u1} [Fig. 2(b)] and L_{u3}/L_{u2} [Fig. 2(c)] are well below unity for both ASL and CSL flows and do not vary appreciably with ζ. Roughly, L_{u1} is about a factor of 10 larger than L_{u3} (shown as a dashed line) in agreement with prior CSL [57] and ASL [58] experiments. Interestingly, the shape of the normalized energy distribution ellipsoid observed in Fig. 1 is qualitatively similar to the effective eddy sizes but they are not identical. Because L_{u3} is the most restrictive eddy size and partly captures some effects of ζ on elongation or compression of eddy sizes [Fig. 2(a)], the scalewise analysis is to be reported as r/L_{u3} (instead of r/z) for each run. It is also worth noting that r/L_{u3} may be interpreted as normalized time-scale separation given that Taylor's hypothesis equally impacts the numerator and denominator. While Taylor's hypothesis is not expected to be suitable near roughness elements [59] in the CSL, its distortions become less severe beyond $z/h > 2$, the case for the CSL here.

The ensemble-averaged (over ζ) normalized $D_{11}/\overline{2u_1u_1}$, $D_{22}/\overline{2u_2u_2}$, and $D_{33}/\overline{2u_3u_3}$ approaches unity at large rL_{u3}^{-1}, consistent with expectations from stationarity arguments (Fig. 3). However, stationarity appears to be attained at smaller rL_{u3}^{-1} for the CSL when compared to its ASL counterpart. The fact that $D_{11}/\overline{2u_1u_1}$ exhibits an approximate logarithmic region at scales larger than inertial but smaller than scales where $dD_{11}(r)/dr \approx 0$ is not surprising for the ASL, and is consistent with prior theoretical analysis explaining the -1 power law in the longitudinal velocity spectrum at large scales as well as in laboratory studies, field experiments, and large eddy simulations [55,60–68]. Such a logarithmic transition between inertial and $dD_{11}(r)/dr \approx 0$ is much more restricted in scale separation within the CSL.

At about $r/L_{u3} = 1/2$, all velocity component structure functions follow the $r^{2/3}$ K41 scaling, consistent with other ASL experiments [69,70]. However, second-order structure function scaling

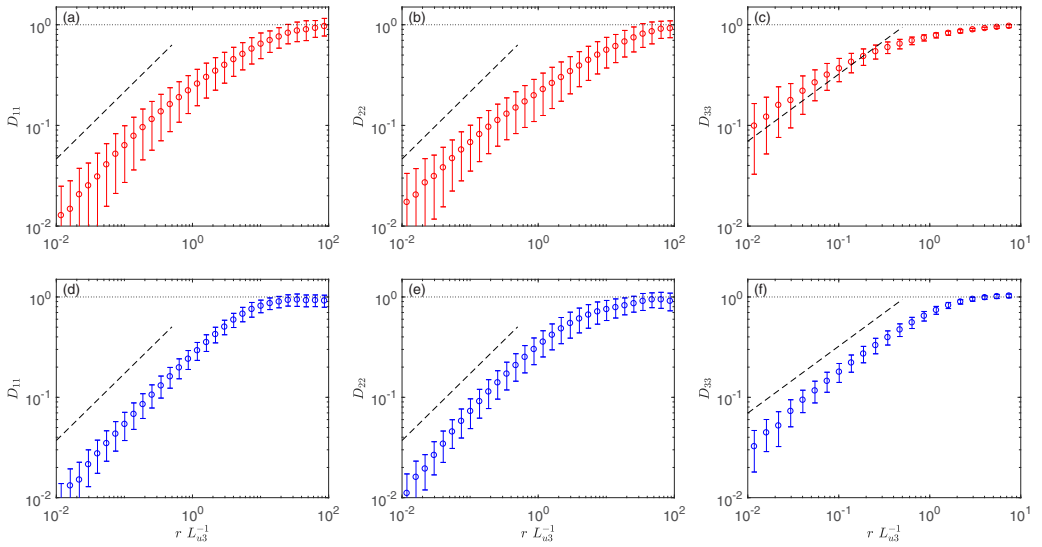

FIG. 3. Ensemble averaged of normalized structure function $\frac{1}{2}D_{11}\overline{u_1u_1}^{-1}$ (left column), $\frac{1}{2}D_{22}\overline{u_2u_2}^{-1}$ (middle column), and $\frac{1}{2}D_{33}\overline{u_3u_3}^{-1}$ (right column) are shown for the ASL (top, red) and CSL (bottom, blue). The black dotted line is $y = 1$ and the black dashed line shows the slope $r^{2/3}$ for Kolmogorov scaling [Eq. (18)]. The error bars show the standard deviation of the ensemble.

laws are only a necessary but not sufficient condition to the attainment of local isotropy. The componentwise velocity structure function ratios against r/L_{u3} demonstrate that anisotropy exists at fine scales even for $r/L_{u3} = 1/2$ and for both ASL and CSL flows (Fig. 4). However, for $r/L_{u3} < 0.1$, predictions from local isotropy agree with measurements. The calculations were repeated for D_{11}/D_{33} and D_{22}/D_{33} to correct for finite squared turbulent intensity effects using the linear model of Wyngaard and Clifford [43,71]. The results do not deviate appreciably from direct application of Taylor's frozen turbulence hypothesis, assuming small turbulent intensity (figure not shown). It is precisely the nature of this anisotropy that we seek to address using the invariance measures across scales.

B. Invariant analysis

The return-to-isotropy trajectories are shown in BAM for all ensemble members [Figs. 5(a) and 5(b)]. The starting and ending points of the scalewise trajectories are consistent with the conventional analysis previously discussed: large scales are further away from the isotropic (or 3D) limit for the ASL when compared to the CSL. The ζ variations also show no significant influence on the starting position of the points within the BAM [Figs. 5(a) and 5(b)].

The relaxation trajectories towards the isotropic (or 3D) state with decreasing scale r appear to be shorter for the CSL when compared to the ASL. Trajectories, by and large, show a return to isotropy by a contraction in the proximity of the 2D-3D limit for near-neutral and unstable ζ. However, the trajectory for stable conditions is closer to the center of the BAM [Figs. 5(c) and 5(d)]. In all cases, meandering of trajectories in the BAM with decreasing scale deviates from predictions based on zero-mean shear or homogeneous turbulence. These deviations partly reflect contributions from dU/dz that is active on all scales. In the AIM, the trajectories show rough similarities in curvature to the model for homogeneous turbulence [Eq. (24)] at the same starting position. This agreement is mainly due to the compressed trajectory representation of AIM near the isotropic limit corner, as discussed elsewhere [32]. The deviation between modeled and measured trajectories is quantified as the shortest distance in the BAM for a given r by $d(dI_2/dI_3, \vec{n}_{\mathrm{BAM}})$, with $\vec{n}_{\mathrm{BAM}} = (x_{\mathrm{BAM}}, y_{\mathrm{BAM}})$ given by Eq. (12) and dI_2/dI_3 by Eq. (24). The ensemble average of the deviation is decreasing

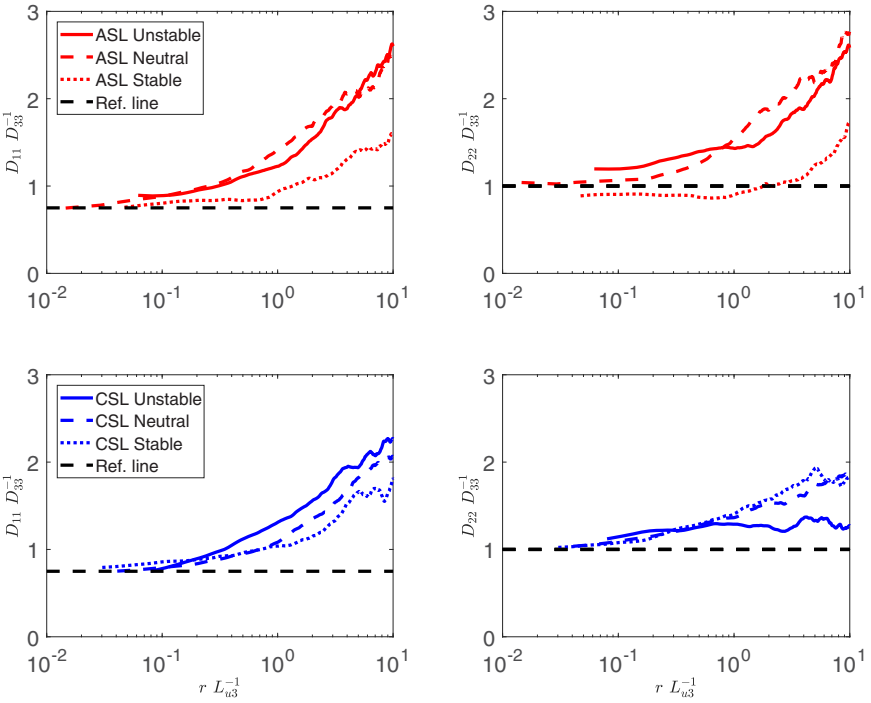

FIG. 4. Local isotropy attained by the ratios $D_{11}D_{33}^{-1}$ (left column) and $D_{22}D_{33}^{-1}$ (right column) for the ASL (top row, red) and CSL (bottom row, blue). The three lines show one example interval for stable (solid), neutral (dashed), and unstable (dotted) conditions. The black dashed line shows the expected ratio for locally isotropic turbulence based on K41.

towards the large scales, because we initialized the model with the measurements at the starting point of the trajectory, and at small scales where both converge to the isotropic state [Figs. 5(e) and 5(f)]. In between, the return to isotropy of the Rotta model shows significant deviations from the measurements, which cannot be explained by the measurement errors. The measurement errors were computed empirically by generating 2500 realizations of the anisotropy tensor a_{ij} from the accuracy of the covariance, assuming a normal distribution. Each a_{ij} was then diagonalized to gain a distribution of the eigenvalues and subsequently a distribution of $\vec{n}_{\mathrm{BAM}}$. From this the measurement error is estimated as the standard deviation of the distance between the mean of $\vec{n}_{\mathrm{BAM}}$ (which is equal to measurements) and each ensemble member.

An ensemble average of all runs shows at which rL_{u3}^{-1} the return to isotropy commences and terminates using both F and C_{iso} (Fig. 6). While the F (or AIM) measure suggests near-isotropic conditions at small scales, the C_{iso} (or BAM) measure suggests small but sustained anisotropy at those same small scales. As noted earlier, the AIM compresses the trajectories (and distance) near isotropic states, whereas BAM does not. Consistent with the previous structure function analysis, a near local isotropy at small scales $rL_{u3}^{-1} < 0.5$ is attained where as anisotropy exists at larger scales. The ASL is shown to be more anisotropic at large scales ($rL_{u3}^{-1} > 100$) when compared to the CSL. Both anisotropy measures reveal three separated regimes: scale independent anisotropy at large scales where F and C_{iso} are constantly low but approximately independent of scale (anisotropy is large), a return-to-isotropy regime in which the flow begins to relax towards isotropy as smaller scales are approached, and a third regime where scale-independent near-isotropy at small scales is attained (anisotropy is weak). The upper and lower scales bounding this intermediate regime are hereafter designated as r_{ani} and r_{iso}, respectively. They were determined from the scale r where C_{ani} has reached 90% of maximum isotropy (approaching from large r) in the case of r_{iso} and from the

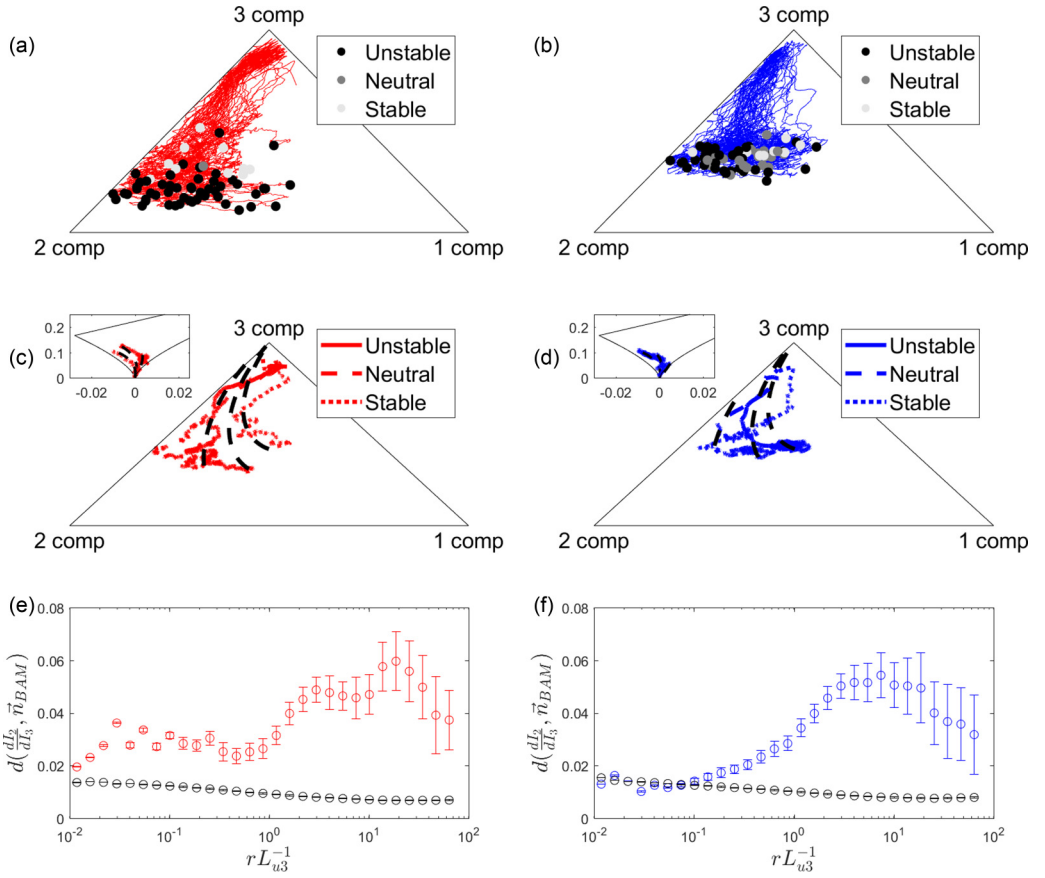

FIG. 5. The top row shows the trajectories of all 30 minute runs for the ASL (a) and the CSL (b) together with starting points color coded according to their stability class (black is unstable, dark grey is near neutral, and light grey is stable). The middle row shows return-to-isotropy trajectories in the BAM for three sample cases with unstable, neutral, and stable stratification of the ASL (c) and CSL (d) together with model trajectories [Eq. (24)]. The insets show the same three trajectories in the AIM representation. The bottom row shows the mean distance between modeled and measured trajectories in BAM, with the standard deviation as error bars, for the ASL (e) and CSL (f) together with the part of each deviation which can be explained by the measurement errors (black).

scale r where C_{ani} was within 10% of its lowest value (approaching from small r) in the case of r_{ani}. In the ASL, the return to isotropy is initiated at larger scales ($r_{\text{ani}} L_{u3}^{-1} > 70$) when compared to the CSL ($r_{\text{ani}} L_{u3}^{-1} > 25$) and covers a wider scale range. The scales at which local isotropy is roughly attained ($r_{\text{iso}} L_{u3}^{-1} = 0.5$) are comparable for the ASL and CSL.

The experiments above urban canopies suggested that r_{ani} varies with an outer length scale associated with the peak in the air temperature spectrum [26]. A similar analysis was conducted using the integral length scale of the air temperature time series L_{uT}, and the outcome is featured in Fig. 7. When analyzing all the individual runs, r_{ani} is smaller for stable than for unstable conditions for the CSL but not the ASL [Fig. 7(a)]. Also, r_{ani} has a weak dependency on L_{uT} for the ASL but not for the CSL [Fig. 7(a)]. In contrast, r_{iso} is less sensitive to variations in L_{uT} [Fig. 7(b)], especially in the ASL ($r_{\text{iso}} \approx z/2$). Normalizing r_{ani} and r_{iso} with L_{u3} removes any L_{uT} dependency in the ASL [Figs. 7(c) and 7(d)] and the correlation coefficient of L_{uT} and r_{ani} decreases from 0.43 to 0.02, and in case of r_{iso} it decreases from 0.40 to -0.12 (in the CSL all correlation coefficients are

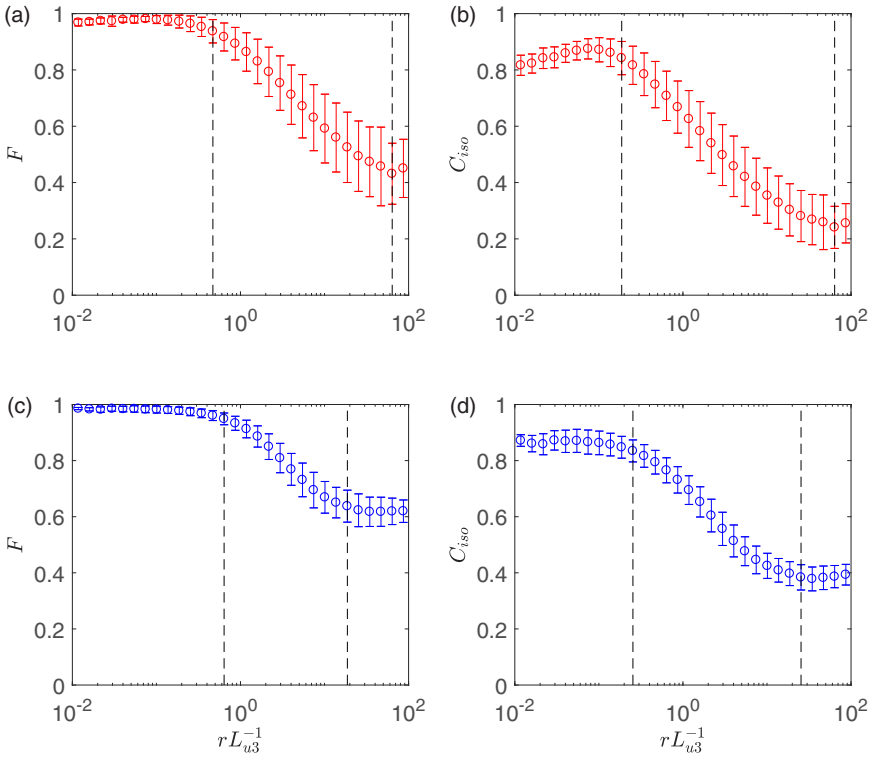

FIG. 6. Anisotropy measures F [left column, Eq. (14)] and C_{ani} [right column, Eq. (15)] are shown for ASL (top row, red) and CSL (bottom rom, blue) as an ensemble average with standard deviation across all ζ to highlight the role of surface roughness. The black dashed lines show three regimes defined by reaching 90% of maximum isotropy or 10% of anisotropy.

smaller than 0.14). That is, much of the dependency of r_{ani} on L_{uT} in the ASL can be attributed to variations in L_{u3} with $-\zeta$. Furthermore, ensemble averages of r_{ani} are significantly different for CSL and ASL and remain significantly different if normalized with L_{u3}. The ensemble average of r_{iso} is also significantly different when comparing CSL and ASL flows, but this difference is collapsed if r_{iso} is normalized L_{u3}. These results are robust even when other methods for determining r_{ani} and r_{iso} (e.g., fitting a tangent hyperbolic function) are employed (not shown). In comparison to experiments above urban canopies [26], values of L_{uT} cover similar ranges in the ASL and CSL. The range r_{ani} covers more than a decade if ASL and CSL results are treated separately (and when excluding the data point with $r_{\text{ani}} = 5$ for the CSL), which is a larger range than observed above urban canopies. It may be surmised that the return to isotropy depends more on roughness properties and less on surface heating or cooling for the same L.

The persistence of anisotropy at small scales has been extensively studied and linked to the finite mean velocity gradient [72,73]. The so-called integral structure function of order n, defined as

$$\overline{\left[\Delta u_k(r)^3 + \alpha_c r \frac{dU}{dz} \Delta u_k(r)^2\right]^{n/3}}, \tag{29}$$

has been shown to recover measured structure functions in laboratory settings and simulations [72,73] at small scales, where α_c is a similarity constant. The prevalence of dU/dz acting on all scales suggests that anisotropy produced by the mean velocity gradient can persist throughout the inertial subrange via finite cospectra [74,75]. This argument was recently suggested to explain persistent anisotropy in the urban surface layer [26]. In terms of a lower boundary condition on the flow, this mean velocity

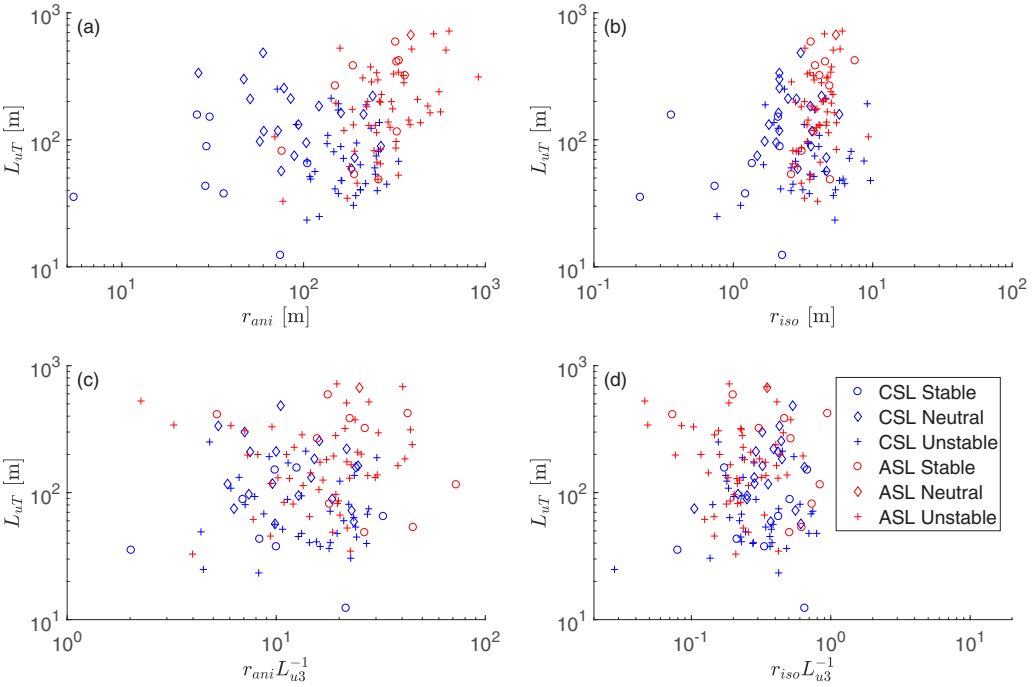

FIG. 7. The starting scales of the return to isotropy r_{ani} (a) and $r_{\text{ani}}L_{u3}^{-1}$ (c) and scales r_{iso} (b) and $r_{\text{iso}}L_{u3}^{-1}$ (d) at which isotropy is reached are plotted against the temperature length scale L_{uT}. Circles indicate stable, diamonds near-neutral, and crosses unstable stratification. Blue symbols show the CSL over the forest canopy and red symbols the ASL over the desert surface.

gradient is linked to the shear stress and thermal stratification by

$$\frac{dU}{dz} = \phi_m(\zeta)\frac{u_*}{\kappa z}. \tag{30}$$

For near-neutral conditions (i.e., $\phi_m(0) = 1$) and at a fixed z, increasing u_* increases dU/dz.

In the case of the CSL, u_* and dU/dz are expected to be higher than their ASL counterpart if κz is similar. However, the invariant analysis here suggests that ASL is more anisotropic at fine scales, $r < r_{\text{iso}}$. Hence, shear intensity (or dU/dz) alone cannot be the main cause. The alternative explanation stems from the fact that $\sigma_{u3}/(\sigma_{u1} + \sigma_{u2})$ is larger for the CSL when compared to its ASL counterpart for similar ζ values. While both ASL and CSL turbulence appear to be isotropic in the plane paralleling the ground surface, the CSL energy ellipsoid appears to be closer to 3D when compared to its ASL counterpart. This initial energy configuration state at large scales in the ASL requires that the return to isotropy transfer more energy to the vertical direction when compared to the CSL.

V. BROADER IMPACTS

The results presented here are pertinent to subgrid-scale turbulence closure schemes in large eddy simulations. Most models use subgrid-scale stress parametrization based on isotropic eddy-diffusivity schemes (e.g., PALM [76–78]). Turbulence closure methods accounting for subgrid-scale anisotropy based on explicit algebraic Reynolds stress models, which utilize the mean strain and rotation rate, have been developed and successfully tested [79,80]. Our results show that near isotropy can be attained for fine scales (<5 m) in CSL and ASL flows, but coarser grid resolutions require anisotropic subgrid modeling. Further, the results here can be utilized to improve or formulate new wall-blocking models, for example in the description of the mean velocity profile [81], as the data set spans

atmospheric flows from weak blockage (CSL) to strong blockage (ASL) and covers a wide range of velocity variances. The aforementioned examples above implicitly or explicitly assume Rotta's energy redistribution hypothesis, which is popular in higher-order closure schemes [82] used in climate and weather forecasting models (e.g., weather research and forecasting model). The analysis here hints of a need for exploring approaches beyond a linear Rotta scheme. Another path for improvement is to find a normalization collapsing r_{ani} between CSL and ASL, which then could be utilized in modeling the efficiency of the return to isotropy.

VI. CONCLUSIONS

Scalewise invariant analysis showed that the return to isotropy is initiated at larger scales and covers a wider range of scales in the ASL when compared to the CSL. This statement holds when scales (or separation distances) are normalized by the integral length of the vertical velocity. The two normalized scales at which the return to isotropy becomes active and near isotropy is attained are insensitive to atmospheric thermal stratification (again when the scales are normalized by the integral length scale of the vertical velocity). However, the precise trajectory in the BAM towards isotropy at finer scales is modified by thermal stratification and mean velocity gradient, and does not follow expectation from homogeneous turbulence. The analysis also reveals that larger scales appear less anisotropic in the CSL when compared to its ASL counterpart. Both CSL and ASL appear to be near-planar isotropic at large scales. However, the reduced overall anisotropy in the CSL mainly originates from $\sigma_{u3}/(\sigma_{u1} + \sigma_{u2})$ being larger for CSL when compared to its ASL counterpart. Hence, CSL turbulence commences its relaxation to isotropy in BAM with reduced scales from a point closer to the 3D state and along the 2D-3D interface. Because of the significance of the third invariant (in both ASL and CSL), the classical Rotta return-to-isotropy approach must be amended. The work here also shows that the return to isotropy depends more on surface roughness properties and less on surface heating. From a broader perspective, the work here extends prior laboratory (pipe and wind-tunnel) studies by demonstrating that rougher surfaces (i.e., a forest) tend to make turbulence more isotropic than their smooth wall or small roughness (i.e., shrubland) counterparts.

ACKNOWLEDGMENTS

G.K. acknowledges support from the National Science Foundation (NSF-EAR-1344703, NSF-AGS-1644382, and NSF-DGE-1068871) and from the Department of Energy (DE-SC0011461). K.K. and P.B. acknowledge support from the German Research Foundation (DFG) as part of the project "Climate feedbacks and benefits of semi-arid forests" (CliFF) (SCHM 2736/2-1). M.M. and F.D.R. acknowledge support from the Helmholtz-Association through the President's Initiative and Networking Fund as part of the Young Investigator Group "Capturing all relevant scales of biosphere-atmosphere exchange—the enigmatic energy balance closure problem" (VH-NG-843). This work was supported by a Helmholtz Research School MICMoR Visiting Scientist Fellowship through KIT/IMK-IFU to G.K. (HGF VH-KO-505).

[1] A. S. Monin and A. M. F. Obukhov, Basic laws of turbulent mixing in the surface layer of the atmosphere, Contrib. Geophys. Inst. Acad. Sci. USSR **24**, 163 (1954) [**151**, e187 (1954)].

[2] A. J. Dyer, A review of flux-profile relationships, Bound.-Lay. Meteorol. **7**, 363 (1974).

[3] J. R. Garratt, Surface influence upon vertical profiles in the atmospheric near-surface layer, Q. J. R. Meteorol. Soc. **106**, 803 (1980).

[4] M. R. Raupach and A. S. Thom, Turbulence in and above plant canopies, Annu. Rev. Fluid Mech. **13**, 97 (1981).

[5] M. R. Raupach, J. J. Finnigan, and Y. Brunet, Coherent eddies and turbulence in vegetation canopies: The mixing-layer analogy, Bound.-Lay. Meteorol. **25**, 351 (1996).

[6] J. J. Finnigan, Turbulence in plant canopies, Annu. Rev. Fluid Mech. **32**, 519 (2000).
[7] T. Foken, 50 years of the Monin–Obukhov similarity theory, Bound.-Lay. Meteorol. **119**, 431 (2006).
[8] I. N. Harman and J. J. Finnigan, A simple unified theory for flow in the canopy and roughness sublayer, Bound.-Lay. Meteorol. **123**, 339 (2007).
[9] G. G. Katul, A. G. Konings, and A. Porporato, Mean Velocity Profile in a Sheared and Thermally Stratified Atmospheric Boundary Layer, Phys. Rev. Lett. **107**, 268502 (2011).
[10] J. C. Wyngaard and O. R. Coté, The budgets of turbulent kinetic energy and temperature variance in the atmospheric surface layer, J. Atmos. Sci. **28**, 190 (1971).
[11] H. A. Panofsky and J. A. Dutton, *Atmospheric Turbulence: Models and Methods for Engineering Applications* (Wiley, New York, 1984).
[12] B. A. Kader and A. M. Yaglom, Mean fields and fluctuation moments in unstably stratified turbulent boundary layers, J. Fluid Mech. **212**, 637 (1990).
[13] J. R. Garratt *et al.*, *The Atmospheric Boundary Layer*, Cambridge Atmospheric and Space Science Series, Vol. 416 (Cambridge University Press, Cambridge, 1994).
[14] J. C. Kaimal and J. J. Finnigan, *Atmospheric Boundary Layer Flows: Their Structure and Measurement* (Oxford University Press, Oxford, 1994).
[15] J. J. Finnigan, R. H. Shaw, and E. G. Patton, Turbulence structure above a vegetation canopy, J. Fluid Mech. **637**, 387 (2009).
[16] T. Banerjee and G. G. Katul, Logarithmic scaling in the longitudinal velocity variance explained by a spectral budget, Phys. Fluids **25**, 125106 (2013).
[17] T. Banerjee, G. G. Katul, S. T. Salesky, and M. Chamecki, Revisiting the formulations for the longitudinal velocity variance in the unstable atmospheric surface layer, Q. J. R. Meteorol. Soc. **141**, 1699 (2015).
[18] T. Banerjee, D. Li, J.-Y. Juang, and G. G. Katul, A spectral budget model for the longitudinal turbulent velocity in the stable atmospheric surface layer, J. Atmos. Sci. **73**, 145 (2016).
[19] E. G. Patton, P. P. Sullivan, R. H. Shaw, J. J. Finnigan, and J. C. Weil, Atmospheric stability influences on coupled boundary layer and canopy turbulence, J. Atmos. Sci. **73**, 1621 (2016).
[20] R. A. Antonia, J. Kim, and L. W. B. Browne, Some characteristics of small-scale turbulence in a turbulent duct flow, J. Fluid Mech. **233**, 369 (1991).
[21] H. S. Shafi and R. A. Antonia, Anisotropy of the Reynolds stresses in a turbulent boundary layer on a rough wall, Exp. Fluids **18**, 213 (1995).
[22] K. S. Choi and J. L. Lumley, The return to isotropy of homogeneous turbulence, J. Fluid Mech. **436**, 59 (2001).
[23] P.-Å. Krogstad and L. E. Torbergsen, Invariant analysis of turbulent pipe flow, Flow, Turbul. Combust. **64**, 161 (2000).
[24] R. A. Antonia and P.-Å. Krogstad, Turbulence structure in boundary layers over different types of surface roughness, Fluid Dyn. Res. **28**, 139 (2001).
[25] R. Smalley, S. Leonardi, R. Antonia, L. Djenidi, and P. Orlandi, Reynolds stress anisotropy of turbulent rough wall layers, Exp. Fluids **33**, 31 (2002).
[26] H. Liu, R. Yuan, J. Mei, J. Sun, Q. Liu, and Y. Wang, Scale properties of anisotropic and isotropic turbulence in the urban surface layer, Bound.-Lay. Meteorol. **165**, 277 (2017).
[27] S. Sarkar and C. G. Speziale, A simple nonlinear model for the return to isotropy in turbulence, Phys. Fluids A **2**, 84 (1990).
[28] P. K. Yeung and James G. Brasseur, The response of isotropic turbulence to isotropic and anisotropic forcing at the large scales, Phys. Fluids A **3**, 884 (1991).
[29] T. Jongen and T. B. Gatski, General explicit algebraic stress relations and best approximation for three-dimensional flows, Int. J. Eng. Sci. **36**, 739 (1998).
[30] F. G. Schmitt, Direct test of a nonlinear constitutive equation for simple turbulent shear flows using DNS data, Commun. Nonlinear Sci. Numer. Simul. **12**, 1251 (2007).
[31] J. P. Panda, H. V. Warrior, S. Maity, A. Mitra, and K. Sasmal, An improved model including length scale anisotropy for the pressure strain correlation of turbulence, J. Fluids Eng. **139**, 044503 (2017).
[32] S. Banerjee, R. Krahl, F. Durst, and C. Zenger, Presentation of anisotropy properties of turbulence, invariants versus eigenvalue approaches, J. Turbul., doi: 10.1080/14685240701506896.

[33] J. L. Lumley and G. R. Newman, The return to isotropy of homogeneous turbulence, J. Fluid Mech. **82**, 161 (1977).
[34] J. L. Lumley, Computational modeling of turbulent flows, Adv. Appl. Mech. **18**, 213 (1979).
[35] T.-H. Shih, J. Zhu, and J. L. Lumley, A new Reynolds stress algebraic equation model, Comput. Methods Appl. Mech. Eng. **125**, 287 (1995).
[36] D. B. Taulbee, An improved algebraic Reynolds stress model and corresponding nonlinear stress model, Phys. Fluids A **4**, 2555 (1992).
[37] T. Rung, F. Thiele, and S. Fu, On the realizability of nonlinear stress–strain relationships for Reynolds stress closures, Flow Turbul. Combust. **60**, 333 (1998).
[38] U. Schumann, Realizability of Reynolds-stress turbulence models, Phys. Fluids **20**, 721 (1977).
[39] D. Poggi, A. Porporato, L. Ridolfi, J. D. Albertson, and G. G. Katul, The effect of vegetation density on canopy sub-layer turbulence, Bound.-Lay. Meteorol. **111**, 565 (2004).
[40] J. M. Chacin and B. J. Cantwell, Dynamics of a low Reynolds number turbulent boundary layer, J. Fluid Mech. **404**, 87 (2000).
[41] S. B. Pope, A more general effective-viscosity hypothesis, J. Fluid Mech. **72**, 331 (1975).
[42] G. I. Taylor, The spectrum of turbulence, Proc. R. Soc. London A **164**, 476 (1938).
[43] C.-I. Hsieh and G. G. Katul, Dissipation methods, taylor's hypothesis, and stability correction functions in the atmospheric surface layer, J. Geophys. Res. **102**, 16391 (1997).
[44] E. Rotenberg and D. Yakir, Distinct patterns of changes in surface energy budget associated with forestation in the semiarid region, Glob. Change Biol. **17**, 1536 (2011).
[45] F. Eder, F. De Roo, E. Rotenberg, D. Yakir, H. P. Schmid, and M. Mauder, Secondary circulations at a solitary forest surrounded by semi-arid shrubland and their impact on eddy-covariance measurements, Agric. For. Meteorol. **211**, 115 (2015).
[46] A. M. Obukhov, The local structure of atmospheric turbulence, Dokl. Akad. Nauk. SSSR **67**, 643 (1949).
[47] U. Högström and A.-S. Smedman, Accuracy of sonic anemometers: laminar wind-tunnel calibrations compared to atmospheric in situ calibrations against a reference instrument, Bound.-Lay. Meteorol. **111**, 33 (2004).
[48] R. G. Barry and R. J. Chorley, *Atmosphere, Weather and Climate*, 8th ed. (Routledge, New York, 2003).
[49] U. Dayan and J. Rodnizki, The temporal behavior of the atmospheric boundary layer in Israel, J. Appl. Meteorol. **38**, 830 (1999).
[50] T. Foken and B. Wichura, Tools for quality assessment of surface-based flux measurements, Agric. For. Meteorol. **78**, 83 (1996).
[51] M. Mauder, M. Cuntz, C. Drüe, A. Graf, C. Rebmann, H. P. Schmid, M. Schmidt, and R. Steinbrecher, A strategy for quality and uncertainty assessment of long-term eddy-covariance measurements, Agric. For. Meteorol. **169**, 122 (2013).
[52] J. C. Isaza and L. R. Collins, On the asymptotic behaviour of large-scale turbulence in homogeneous shear flow, J. Fluid Mech. **637**, 213 (2009).
[53] I. Marusic, J. P. Monty, M. Hultmark, and A. J. Smits, On the logarithmic region in wall turbulence, J. Fluid Mech. **716**, R3 (2013).
[54] C. Meneveau and I. Marusic, Generalized logarithmic law for high-order moments in turbulent boundary layers, J. Fluid Mech. **719**, R1-1 (2013).
[55] R. J. A. M. Stevens, M. Wilczek, and C. Meneveau, Large-eddy simulation study of the logarithmic law for second-and higher-order moments in turbulent wall-bounded flow, J. Fluid Mech. **757**, 888 (2014).
[56] T. Banerjee, P. Brugger, F. De Roo, K. Kröniger, D. Yakir, E. Rotenberg, and M. Mauder, Turbulent transport of energy across a forest and a semi-arid shrubland, Atmos. Chem. Phys. Discuss., doi: 10.5194/acp-2017-159.
[57] G. G. Katul and W.-H. Chang, Principal length scales in second-order closure models for canopy turbulence, J. Appl. Meteorol. **38**, 1631 (1999).
[58] B. A. Kader, A. M. Yaglom, and S. L. Zubkovskii, Spatial correlation functions of surface-layer atmospheric turbulence in neutral stratification, Bound.-Lay. Meteorol. **47**, 233 (1989).

[59] Y. Pan and M. Chamecki, A scaling law for the shear-production range of second-order structure functions, J. Fluid Mech. **801**, 459 (2016).
[60] P. Drobinski, P. Carlotti, R. K. Newsom, R. M. Banta, R. C. Foster, and J.-L. Redelsperger, The structure of the near-neutral atmospheric surface layer, J. Atmos. Sci. **61**, 699 (2004).
[61] P. A. Davidson, T. B. Nickels, and P.-Å. Krogstad, The logarithmic structure function law in wall-layer turbulence, J. Fluid Mech. **550**, 51 (2006).
[62] P. A. Davidson and P.-Å. Krogstad, A simple model for the streamwise fluctuations in the log-law region of a boundary layer, Phys. Fluids **21**, 055105 (2009).
[63] G. G. Katul, A. Porporato, and V. Nikora, Existence of k^{-1} power-law scaling in the equilibrium regions of wall-bounded turbulence explained by Heisenberg's eddy viscosity, Phys. Rev. E **86**, 066311 (2012).
[64] G. G. Katul, T. Banerjee, D. Cava, M. Germano, and A. Porporato, Generalized logarithmic scaling for high-order moments of the longitudinal velocity component explained by the random sweeping decorrelation hypothesis, Phys. Fluids **28**, 095104 (2016).
[65] P. A. Davidson and P.-Å. Krogstad, A universal scaling for low-order structure functions in the log-law region of smooth-and rough-wall boundary layers, J. Fluid Mech. **752**, 140 (2014).
[66] C. M. de Silva, I. Marusic, J. D. Woodcock, and C. Meneveau, Scaling of second-and higher-order structure functions in turbulent boundary layers, J. Fluid Mech. **769**, 654 (2015).
[67] R. A. Antonia and M. R. Raupach, Spectral scaling in a high Reynolds number laboratory boundary layer, Bound.-Lay. Meteorol. **65**, 289 (1993).
[68] Marcelo Chamecki, Nelson L. Dias, Scott T. Salesky, and Ying Pan, Scaling laws for the longitudinal structure function in the atmospheric surface layer, J. Atmos. Sci. **74**, 1127 (2017).
[69] J. C. Kaimal, J. C. Wyngaard, Y. Izumi, and O. R. Coté, Spectral characteristics of surface-layer turbulence, Q. J. R. Meteorol. Soc. **98**, 563 (1972).
[70] G. G. Katul, C.-I. Hsieh, and J. Sigmon, Energy-inertial scale interactions for velocity and temperature in the unstable atmospheric surface layer, Bound.-Lay. Meteorol. **82**, 49 (1997).
[71] J. C. Wyngaard and S. F. Clifford, Taylor's hypothesis and high-frequency turbulence spectra, J. Atmos. Sci. **34**, 922 (1977).
[72] F. Toschi, E. Leveque, and G. Ruiz-Chavarria, Shear Effects in Nonhomogeneous Turbulence, Phys. Rev. Lett. **85**, 1436 (2000).
[73] D. Poggi, A. Porporato, and L. Ridolfi, Analysis of the small-scale structure of turbulence on smooth and rough walls, Phys. Fluids **15**, 35 (2003).
[74] G. G. Katul, A. Porporato, C. Manes, and C. Meneveau, Co-spectrum and mean velocity in turbulent boundary layers, Phys. Fluids **25**, 091702 (2013).
[75] T. Ishihara, K. Yoshida, and Y. Kaneda, Anisotropic Velocity Correlation Spectrum at Small Scales in a Homogeneous Turbulent Shear Flow, Phys. Rev. Lett. **88**, 154501 (2002).
[76] J. W. Deardorff, Stratocumulus-capped mixed layers derived from a three-dimensional model, Bound.-Lay. Meteorol. **18**, 495 (1980).
[77] C.-H. Moeng and J. C. Wyngaard, Spectral analysis of large-eddy simulations of the convective boundary layer, J. Atmos. Sci. **45**, 3573 (1988).
[78] B. Maronga, M. Gryschka, R. Heinze, F. Hoffmann, F. Kanani-Sühring, M. Keck, K. Ketelsen, M. O. Letzel, M. Sühring, and S. Raasch, The parallelized large-eddy simulation model (PALM) version 4.0 for atmospheric and oceanic flows: Model formulation, recent developments, and future perspectives, Geosci. Model Dev. **8**, 2515 (2015).
[79] T. B. Gatski and C. G. Speziale, On explicit algebraic stress models for complex turbulent flows, J. Fluid Mech. **254**, 59 (1993).
[80] L. Marstorp, G. Brethouwer, O. Grundestam, and A. V. Johansson, Explicit algebraic subgrid stress models with application to rotating channel flow, J. Fluid Mech. **639**, 403 (2009).
[81] K. A. McColl, G. G. Katul, P. Gentine, and D. Entekhabi, Mean-velocity profile of smooth channel flow explained by a cospectral budget model with wall-blockage, Phys. Fluids **28**, 035107 (2016).
[82] G. L. Mellor and T. Yamada, Development of a turbulence closure model for geophysical fluid problems, Rev. Geophys. **20**, 851 (1982).